PHOTONICS Research

Full-Stokes polarization transformations and time sequence metasurface holographic display

Shifei Zhang,[1] Lingling Huang,[1,*] Guangzhou Geng,[2] Junjie Li,[2] Xiaowei Li,[3] and Yongtian Wang[1]

[1]Beijing Engineering Research Center of Mixed Reality and Advanced Display, School of Optics and Photonics, Beijing Institute of Technology, Beijing 100081, China
[2]Institute of Physics, Chinese Academy of Sciences, Beijing 100191, China
[3]Laser Micro/Nano-Fabrication Laboratory, School of Mechanical Engineering, Beijing Institute of Technology, Beijing 100081, China
*Corresponding author: huanglingling@bit.edu.cn

Received 7 December 2021; revised 18 February 2022; accepted 18 February 2022; posted 22 February 2022 (Doc. ID 450354); published 25 March 2022

With the development of micro/nano fabrication technology, metasurface holography has emerged as a revolutionary technology for the manipulation of light with excellent performance. However, for applications of full-Stokes polarization encryption and time sequence holographic display, multiplexing strategies of metasurfaces with large bandwidths and simple operations still need to be developed. As one of the most popular schemes of multiplexing, polarization multiplexed metasurfaces have shown flexible recording abilities for both free-space beam and surface waves. Here, by using a dielectric metasurface equipped with double phase holograms, we have achieved flexible polarization multiplexed transformations from one full-Stokes space to another. The vectorial hologram is optimized by a hybrid genetic algorithm and digitalized with subwavelength modulated units. Based on a quantitative map and remarkable information capacity, time sequence holographic display and complex optical encryption are experimentally demonstrated by changing input/output polarization channels in real time. We believe our method will facilitate applications in smart compact devices of dynamic display, dynamic optical manipulation, optical encryption, anticounterfeiting, etc.

https://doi.org/10.1364/PRJ.450354

1. INTRODUCTION

As a technique to fully engineer the wavefronts of light, holography has demonstrated remarkable modulation abilities for both free-space beams [1–4] and surface waves [5–7], and facilitated applications of wavefront shaping, data storage, three-dimensional display, and so on. However, for optical holographic video display and complex optical encryption, the bandwidth is still limited, and undesired diffraction orders exist in using traditional approaches. The metasurface, proposed as a novel artificial planar element with subwavelength units, has become a powerful platform for hologram recording in recent years. It can overcome the above limitations and also provide unprecedented spatial resolution and a large field of view (FOV). Over the past decade, delicately designed meta-atoms have shown flexible light manipulation properties, such as amplitude [6,8–13], phase [8–15], polarization [14,16–21], orbital angular momentum (OAM) [22–26], and frequency [12,25,27–31]. Through coding the meta-atoms with diverse holograms in different optical channels, holographic information capacity can be further augmented, and multiplexed functions are available [8,10–14,17–27,31–33].

Among the fundamental light properties, polarization records the vectorial nature of light containing rich invisible information to human eyes. Due to the unique advantages of metasurfaces in designing anisotropic optical response, polarization multiplexed holography based on various metasurface design strategies has emerged [8–12,14,18–21,25,34–37], and greatly promotes potential applications such as optical document security and optical switching devices. However, most schemes are dependent on orthogonal polarization states [14,19,21,24], rather than using all states on the full Poincaré sphere, which decreases the versality and information capacity of polarization multiplexed holography. As one of the most widely used strategies, the spatial multiplexing method [8,20,34,35] relying on supercells suffers from low conversion efficiency and undesired diffraction orders. Especially for supercell metasurfaces tailored by the detour phase [8,14,36], oblique incidence becomes necessary and does not adapt to applications working under normal illumination. So far, progress has put forward challenging requirements for an advanced encoding method and more delicate metasurface design

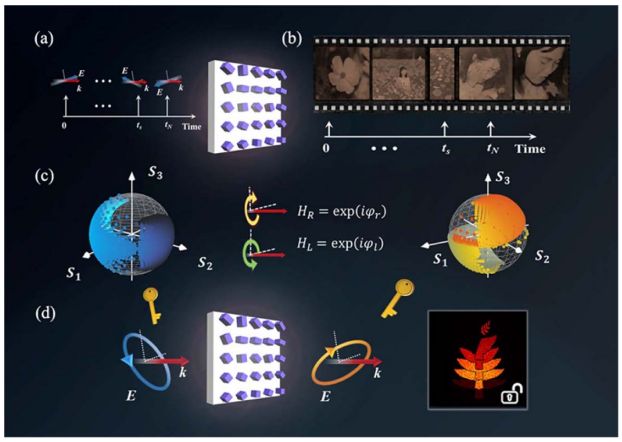

Fig. 1. Principle of polarization multiplexed holography for time sequence holographic video and optical encryption based on metasurfaces. (a) Time-dependent image frames encoded in diverse linear polarization states ranging from zero to π. (b) Holographic video display addressed by varied input and fixed output polarizations. (c) Flexible mapping from the input Poincaré sphere to the output Poincaré sphere, available by designing the phase-only holograms of RCP and LCP channels. (d) Optical encryption that uses input and output polarization states as double secret keys.

to achieve greater polarization modulation possibilities, more information capacity, and high conversion efficiency.

Here, we propose a novel metasurface encoding method to achieve polarization multiplexed holography, which can realize diverse holographic mappings from one full-Stokes space to another efficiently with subwavelength units. As shown in Fig. 1, based on metasurfaces encoded with vectorial holograms with unbounded possibilities, we can selectively address the intensity distributions in the transmitted field according to input and output polarization states, which greatly improves the availability of polarization modes and information capacity. The delicately designed metasurfaces have high polarization conversion in the circular polarization channels, and can achieve independent phase modulations that combine dynamic phase and geometric phase. With the help of a hybrid genetic algorithm, we generated phase-only holograms to synthesize multiple vectorial fields based on the designed meta-atoms. By loading the time-varying polarization channels in sequence, a holographic video and complex optical encryption with double secret keys have been experimentally demonstrated in real time. Such a scheme opens new avenues for multi customizable polarization modulations, and is expected to be used in dynamic display, dynamic optical manipulation, optical encryption, and anticounterfeiting.

2. RESULTS AND DISCUSSION

A. Principle of Polarization Multiplexed Holography

Mathematically, at a given input polarization $|p_0^{\text{in}}\rangle$, the polarization multiplexed hologram can be expressed as the superposition of sub-holograms with diverse polarization states: $H^{\text{mul}} = \sum A_j e^{i\psi_j}|p_j^{\text{out}}\rangle$, where A_j, $e^{i\psi_j}$, and $|p_j^{\text{out}}\rangle$ represent the amplitude, phase, and polarization state of the jth hologram. Here, we utilize the interaction of the input polarized plane wave and metasurface to construct H^{mul}, which satisfies the relationship $H^{\text{mul}} = J|p_0^{\text{in}}\rangle$, and J is the 2×2 Jones matrix of metasurfaces at each pixel. As we build the vectorial images in the far field, the reconstructed field E_{rec} can be regarded as the Fourier transform of H^{mul}, namely, $E_{\text{rec}} = \mathfrak{F}(\sum A_j e^{i\psi_j}|p_j^{\text{out}}\rangle)$, where $\mathfrak{F}$ is the Fourier transform operator. Polarization state $|p_j^{\text{out}}\rangle$ connected with the jth hologram is independent of the spatial coordinate and not involved in the process of Fourier transform, so we can recast the reconstructed field as $E_{\text{rec}} = \sum \mathfrak{F}(A_j e^{i\psi_j})|p_j^{\text{out}}\rangle$ according to the linear property of Fourier transform. By imposing polarization selection $|p_s\rangle$ to the whole field with a spatial inhomogeneous vectorial nature, we can modulate the optical field E and intensity distribution I to $\sum \mathfrak{F}(A_j e^{i\psi_j})\langle p_s|p_j^{\text{out}}\rangle|p_s\rangle$ and $|\sum \mathfrak{F}(A_j e^{i\psi_j})\langle p_s|p_j^{\text{out}}\rangle|^2$, respectively. Clearly, the intensity of each vectorial component is governed by the polarization correlation, and the polarization of the sub-image with maximum intensity distribution is consistent with $|p_s\rangle$. Thus, a holographic mapping from customized $|p_0^{\text{in}}\rangle$ to diverse $|p_s\rangle$ is available for optical data storage and information processing. By simplifying the 2×2 Jones matrix of nanostructures into two off-diagonal components, we can further build the holographic connections between diverse input polarization states and specific output polarization selections clearly.

Next, we describe the recording rules of vectorial holography to achieve dynamic modulations by diverse input/output polarization channels. Since arbitrary $|p_j^{\text{out}}\rangle$ is described by two orthogonally polarized vectors, at least two polarization channels are required to digitize the vectorial holography. We decomposed the vectorial holography into two circularly polarized holograms, which can be recorded with metasurfaces in subwavelength pixels commendably. The complex-amplitude holograms of right circular polarization (RCP) and left circular polarization (LCP) channels can be expressed as $H_R = \sum A_j e^{i\psi_j}\langle R|p_j^{\text{out}}\rangle$ and $H_L = \sum A_j e^{i\psi_j}\langle L|p_j^{\text{out}}\rangle$, respectively, where $\langle R|$ and $\langle L|$ are the left vector of RCP and LCP, respectively. On the other hand, the phase-only holograms of RCP and LCP channels can be described as $H'_R = \exp(i\psi_r)$ and $H'_L = \exp(i\psi_l)$, respectively, where $\psi_r = \arg(\sum A_j e^{i\psi_j}\langle R|p_j^{\text{out}}\rangle)$ and $\psi_l = \arg(\sum A_j e^{i\psi_j}\langle L|p_j^{\text{out}}\rangle)$ in some cases. To efficiently reconstruct the desired field, the final phase-only holograms H'_R and H'_L are usually provided by suitable optimization algorithms. Obviously, the reconstructed field in the far field decomposed as $E_{\text{rec}} = E_R|R\rangle + E_L|L\rangle$ satisfies the conditions as $E_R = \mathfrak{F}(H_R)$ and $E_L = \mathfrak{F}(H_L)$, where E_R and E_L are the complex amplitude fields of RCP and LCP channels in the far field, respectively. We purposely designed the metasurface as a transmitted half-wave plate with sufficient phase modulation capacity, whose Jones matrix can be described as the following equation in the circular polarization basis:

$$J = \begin{bmatrix} t_{rr} & t_{rl} \\ t_{lr} & t_{ll} \end{bmatrix} = \begin{bmatrix} 0 & e^{i\varphi_r} \\ e^{i\varphi_l} & 0 \end{bmatrix}, \tag{1}$$

where t_{rl} is the transmission coefficient of $|L\rangle$ input / $|R\rangle$ output and so are others, and φ_r and φ_l correspond to the phase response of the modulation channels t_{rl} and t_{lr}, respectively. In this case, the meta-atoms have total circular polarization conversion and full-range phase modulation. According to $H^{\text{mul}} = J|p_0^{\text{in}}\rangle$, we can get the relationship between the holograms with the input as $H_R = e^{i\varphi_r}\langle L|p_0^{\text{in}}\rangle$ and $H_L =$

$e^{i\varphi_l}\langle R|p_0^{\text{in}}\rangle$, where $\langle L|p_0^{\text{in}}\rangle$ represents the LCP component of $|p_0^{\text{in}}\rangle$ and so is $\langle R|p_0^{\text{in}}\rangle$. Here, we set the initial input polarization $|p_0^{\text{in}}\rangle$ as x polarized; in this case, the metasurface can simultaneously record both phase-only holograms in t_{rl} and t_{lr} polarization channels. That is, $e^{i\varphi_r} = H'_R$ and $e^{i\varphi_l} = H'_L$, which can be obtained by a specific optimization algorithm. In a sense, we can use H_R and H_L to express the off-diagonal components of the Jones matrix approximately, which can help to better analyze the modulation effect of the input polarized field.

When we use another polarized input $|p_\kappa^{\text{in}}\rangle$ to interact with metasurfaces, the output RCP and LCP holograms become $H_R\langle L|p_\kappa^{\text{in}}\rangle$ and $H_L\langle R|p_\kappa^{\text{in}}\rangle$ approximately, and the synthetic multiplexed hologram H_κ^{mul} at input $|p_\kappa^{\text{in}}\rangle$ can be expressed as

$$H_\kappa^{\text{mul}} \approx \sum A_j e^{i\psi_j}\begin{bmatrix}\langle R|p_j^{\text{out}}\rangle\langle L|p_\kappa^{\text{in}}\rangle \\ \langle L|p_j^{\text{out}}\rangle\langle R|p_\kappa^{\text{in}}\rangle\end{bmatrix} = \sum A_j e^{i\psi_j}|p_{j\kappa}^{\text{out}}\rangle, \quad \textbf{(2)}$$

where $|p_{j\kappa}^{\text{out}}\rangle$ represents the generated output polarization state of the jth hologram at input polarization state $|p_\kappa^{\text{in}}\rangle$. After the far-field reconstruction and output polarization selections, the output field changes to $\sum \mathfrak{T}(A_j e^{i\psi_j})\langle p_s|p_{j\kappa}^{\text{out}}\rangle|p_s\rangle$, and the intensity distribution changes to $|\sum \mathfrak{T}(A_j e^{i\psi_j})\langle p_s|p_{j\kappa}^{\text{out}}\rangle|^2$. Therefore, a bridge of polarization multiplexed holography has been built between the input polarization states and output polarization selections. Note that, albeit the polarization mapping is flexible between the two polarization spaces, the mapping of the same circular polarization is forbidden, which results from the zero energies in t_{rr} and t_{ll} polarization channels based on the designed Jones matrix. On the other hand, the multiplexing capacity has been greatly enhanced, and novel applications are expected.

B. Metasurface Design

Next, we introduce the design strategy of metasurface digitalization. First, we developed an efficient approach to design meta-atoms with separated and sufficient phase modulations in t_{rl} and t_{lr} channels. As the most popular method of metasurface designs, geometric phase, also known as Pancharatnam–Berry (PB) phase, utilizes polarization evolution to realize continuous phase modulation ability related to azimuthal rotations. For meta-atoms with rotation angle θ, a phase response $\pm 2\theta$ can be introduced to t_{rl} and t_{lr}, respectively. To make the phase modulation of t_{rl} and t_{lr} independent, we integrated geometric phase together with dynamic phase. We chose amorphous silicon (α-Si) nanofins with rectangular cross sections as modulated units, which have excellent optical response in the near infrared band and the same dynamic phase response θ_0 in t_{rl} and t_{lr} channels resulting from geometric symmetry. That is, the φ_r and φ_l of each modulated unit are equal to $\theta_0 + 2\theta$ and $\theta_0 - 2\theta$, respectively, where θ_0 can be tailored by the change of geometric cross sections. We conducted a parameter sweep of α-Si nanofins with diverse cross sections by the rigorous coupled wave analysis (RCWA) method to determine suitable structures. The period and height are fixed at 400 nm and 600 nm, respectively, the refractive index we used for calculation is $3.85 + 0.01i$ at a wavelength of 800 nm, and the sweeping range of the width and length is from 80 nm to 240 nm. The amplitude response and the calculated dynamic phase of the t_{rl} channel are shown in Fig. 2(b). Among the nanofins with amplitude response $|t_{rl}|$ above 0.83, 56 structures were selected to cover a full phase range at the same time. Afterwards, by rotating the selected nanofins, we got an effective database to encode each separate hologram.

Then we designed a hybrid genetic algorithm to calculate the phase-only holograms of RCP and LCP channels based on the structural database. As shown in Fig. 2(c), we first generated the initial metasurface by randomly setting the lengths, widths, and rotations based on the above nanofins. The constructed fields of both circularly polarized channels E_R and E_L can be calculated based on diffraction theory. To reconstruct the vectorial images, we have three target parameters: intensity distribution I_j, polarization components $\langle R|P_j^{\text{out}}\rangle$ and $\langle L|P_j^{\text{out}}\rangle$ of all images, and the design degrees of freedom (DOFs) containing only two phase distributions H'_R and H'_L. In this case, we nested an alternative selection in the iterative loops to manipulate more parameters by a few ones. The idea is that if the number of target parameters M is larger than the number of DOFs Q, at least M/Q (a nature number rounded up) alternative selections are nested in the iterative loop. Here, we need to nest the selections only twice. The complete loop begins with the odd iteration number (iterative number $n = 2q - 1$; q is positive integer), and in this case, we selected the absolute phase of $E_R(n)$ as the imaging phase $\varphi(n)$. With the later replacement of target intensities I_j and polarization distributions $\langle R|P_j^{\text{out}}\rangle$ and $\langle L|P_j^{\text{out}}\rangle$, the next holograms can be generated by inverse Fourier transform and nanofin digitalization. The iteration number becomes even ($n = 2q$), and in this selection process, we chose the absolute phase of calculated $E_L(n)$ as $\varphi(n)$, which has the characteristic of previous $E_R(2q - 1)$ and target fields. The replacement process was kept the same as in the previous step. Through the hybrid iteration, both characteristics of the two polarization channels can be preserved based on the above database of nanofins. Therefore, holography recording based on metasurfaces is algorithmically realized.

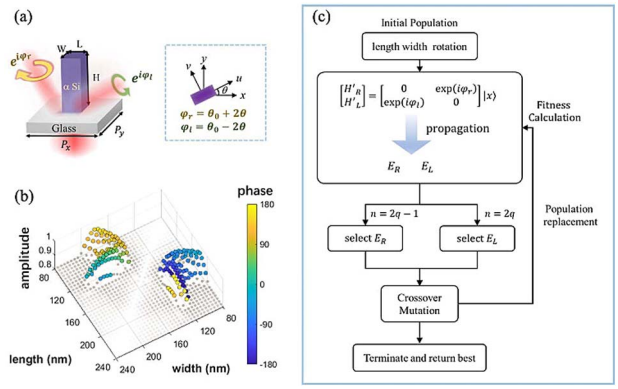

Fig. 2. Metasurface design and digitalization based on hybrid genetic algorithm. (a) Schematic illustration of phase modulation by combining dynamic phase and geometric phase. (b) Simulated results for the amplitude and dynamic phase of t_{rl} channel. The selected nanofins are marked by colored dots, with various phases ranging from $-\pi$ to π and high amplitude above 0.83. (c) Flowchart of the hybrid genetic algorithm for generating metasurfaces based on the selected structures, where n is an integer that represents the parity of iteration number.

C. Experimental Characterizations

We designed and fabricated two metasurfaces to demonstrate our method. As described in Fig. 1, the first is the time sequence holographic display of a prose poem, and the second is an optical encryption composed of a metasurface and two separate keys. Nano fabrication depends on the standard electron beam lithography and inductively coupled plasma reactive ion etching process. Scanning electron microscopy images of sample 1 (dynamic display) and sample 2 (optical encryption) are shown in Fig. 3(a) and Fig. 3(b). Both metasurfaces have a footprint of 480 μm × 480 μm. By using the experimental setup shown in Fig. 3(c), we collected holographic images at diverse input/output polarization selections.

1. Time Sequence Holographic Video

To facilitate practical application, we encoded the time-dependent frames with linearly polarized input that orbits around the equator of the Poincaré sphere, and the analyzer in the output space was fixed without any adjustment. For the jth word of the poem, we designed various phase delays $\pm\varphi_j$ into the RCP and LCP holograms, which helps to create the multiplexed sequence. At the initial x-polarized incidence, the output poem is composed of diverse linearly polarized words $\sum_j^N \sqrt{I_j(x,y,z)}|p_j^{\text{out}}\rangle$ before modulation of the analyzer, where I_j is the intensity distribution of the jth part, N is the total number of words and equals 16, and $|p_j^{\text{out}}\rangle = \frac{1}{\sqrt{2}}[\,e^{i\varphi_j} \quad e^{-i\varphi_j}\,]^T$ in the circularly polarized basis $[|R\rangle, |L\rangle]$. We changed the input linear polarization angle and described it with α (that is, $|p_\kappa^{\text{in}}\rangle = [e^{i\alpha}, e^{-i\alpha}]^T$), and the linear polarization angle of the analyzer was set as β ($|p_s\rangle = [e^{i\beta}, e^{-i\beta}]^T$). The collected intensity of the jth vectorial component at this input/output polarization channel can be calculated based on the above principles, which can be expressed as

$$I_{s\kappa,j} = I_j \cos^2(\varphi_j - \alpha - \beta). \tag{3}$$

Here, we make β be zero, and φ_j in the poem ranges from 0° to 180°. Thus, when the incident α changes from 0° to 180°, the word with maximum intensity can be selectively addressed in sequence. The designed metasurface is composed of 1200 × 1200 nanofins, with different cross sections and rotations optimized by the hybrid genetic algorithm. As shown in Fig. 3(c), we used P_1 and a half-wave plate to generate varied linearly polarized light, and in the output, we removed the quarter-wave plate and fixed P_2 as x polarized. The simulated and experimental results shown in Fig. 4(c) are consistent with the theoretical design; the poem is dynamically displayed by varying the incident polarization angle α, following the order of designed φ_j. In addition, the collected profile of the $|L\rangle$ input / $|R\rangle$ output channel shows uniform distribution of each word, and the detected signals of t_{rr} and t_{ll} channels are relatively weak (see Fig. 6 in Appendix A).

Above all, the dynamic display of holographic videos with high performance has been experimentally realized. It does not require adjustment of the analyzer at the output end, which is more practical for system integration. By increasing the multiplexed number, the movie can be encoded with more information. Furthermore, different display requirements are also available by the polarization multiplexed strategy. For example, for videos played in linearly polarized input/output channels, the display time of sub-images can be precisely customized according to the ellipticity, and real-time editing, rewinding, and inserting of the movie can be easily realized based on diverse polarization selections. Compared with other multiplexed schemes, such as utilizing incident wavelength, OAM, and nonlinear frequencies as multiplexing parameters, the polarization multiplexed strategy shows the advantage of simple manipulation. Various functionalities can be realized by modulating the input/output polarizations. In contrast, nonlinear frequency multiplexing needs high incident intensity, large nonlinear susceptibility, and a complex design to meet phase matching conditions. OAM multiplexing relies on a spatially distributed phase profile generated from spiral plates or spatial light modulators. Furthermore, polarization multiplexing based

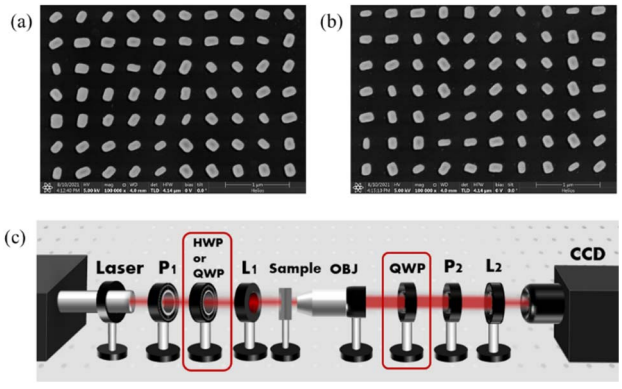

Fig. 3. Scanning electron microscopy images of the fabricated samples and the experimental setup. (a), (b) Scanning electron microscopy images of sample 1 (time sequence holographic video) and sample 2 (optical encryption), composed of diverse cross sections and rotations. (c) Experimental setup for vectorial holography, which works at various input/output polarization channels. P_1 and P_2, polarizers; HWP, half-wave plate; QWP, quarter-wave plate; L_1 and L_2, lenses; OBJ, objective.

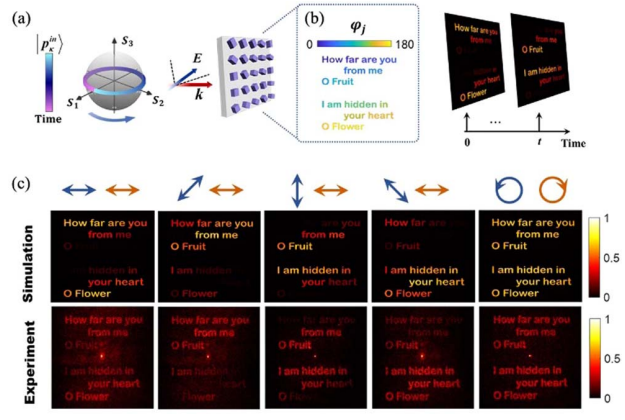

Fig. 4. Design principle of the time sequence holographic video of Tagore's poem. (a) Time-dependent frames encoded in the linearly polarized input, which round the equator of the Poincaré sphere. (b) The preset phase modulation φ_j of the jth word covers 0°–180°, and 16 vectorial words would be generated in one polarization modulation period. (c) Simulated and experimental results for dynamic display; blue polarization states represent the input, and orange states represent the output (see Visualization 1).

on our method can facilitate applications of compact devices with the integration of liquid crystal.

2. Optical Encryption with High Complexity

The first design mainly depends on linear polarization multiplexing of input/output channels. In the second design, we extended the polarization modulation range to the full-Stokes space, and a demonstration of optical encryption with high security is provided as follows. The secret information is hidden in multiple polarization multiplexed images, which has many possibilities due to distinct input/output polarization selections. As shown in Fig. 5(b), the designed pattern of a dove with five wings and leaves has seven polarization states, which can convert an arbitrary incident polarization state (except for circular polarization states) into different polarization states in the output full-Stokes space. Upon x-polarized incidence, we describe the vectorial dove as $\sum_j^7 \sqrt{I_j(x,y,z)}|p_j^{\text{out}}\rangle$, where $|p_j^{\text{out}}\rangle = [\cos\chi_j e^{i\varphi_j}, \sin\chi_j e^{-i\varphi_j}]^T$, and χ_j and φ_j imply the changes of amplitude and phase in circularly polarized channels, respectively. Next, we change input polarization to another state $|p_\kappa^{\text{in}}\rangle$, and the constructed vectorial field becomes $\sum\sqrt{I_j(x,y,z)}[\cos\chi_j e^{i\varphi_j}\langle L|p_\kappa^{\text{in}}\rangle, \sin\chi_j e^{-i\varphi_j}\langle R|p_\kappa^{\text{in}}\rangle]^T$. That is, the generated vectorial field and the output intensity of each sub-image change upon different illuminance conditions except for linearly polarized input. With further decoding with an analyzer that can be expressed as $|p_s\rangle\langle p_s|$, we can get a reliable tool to encode the secret information into polarization multiplexed images. The intensity distribution of the jth vectorial component at the $|p_\kappa^{\text{in}}\rangle$ input / $|p_s\rangle$ output polarization channel can be expressed as follows:

$$I_{s\kappa,j} = I_j(\cos\chi_j C_{s\kappa} + \sin\chi_j C'_{s\kappa})^2, \tag{4}$$

where $C_{s\kappa}$ and $C'_{s\kappa}$ are two coefficients related to polarization selections $C_{s\kappa} = \langle p_s|R\rangle\langle L|p_\kappa^{\text{in}}\rangle$ and $C'_{s\kappa} = \langle p_s|L\rangle\langle R|p_\kappa^{\text{in}}\rangle$, respectively. We set χ_j and φ_j of different vectorial parts as [90°, 0°, 52.5°, 45°, 45°, 45°, 67.5°] and [0°, 0°, 45°, 0°, 60°, 90°, −45°] from top to bottom, respectively, which is shown in Fig. 5(b). Thus, the leaves in the upper right corner are the RCP state, and the upper left wing is the LCP state. The first two columns of experimental results in Fig. 5(e) demonstrate the encoding of phase-only holograms in circular polarization channels, which are essential for constructing multiple polarized images in momentum space.

For the use of optical encryption, we set the first secret key as x-polarized incidence. When using the first secret key to interact with the metasurface, all vectorial patterns are displayed in Fig. 5(c). The second secret key is set as y polarized, which is expected to show brighter third and fourth wings and the absence of second wings; the experimental result in the third column of Fig. 5(e) is consistent with the theoretical design. Furthermore, much deceptive information can be realized at other input/output polarization channels (results at more input/output polarization selections are provided in Figs. 7 and 8, Appendix A). Since the proposed encoding rules are based on the linear additivity of Fourier transformation, it is more suitable for large capacity information multiplexing compared with other schemes. The polarization states of input and output as secret keys have innumerable possibilities in the full-Stokes space, and the complexity and security of such optical encryption are extremely high, especially when the three elements (metasurfaces and two secret keys) are preserved and transferred separately.

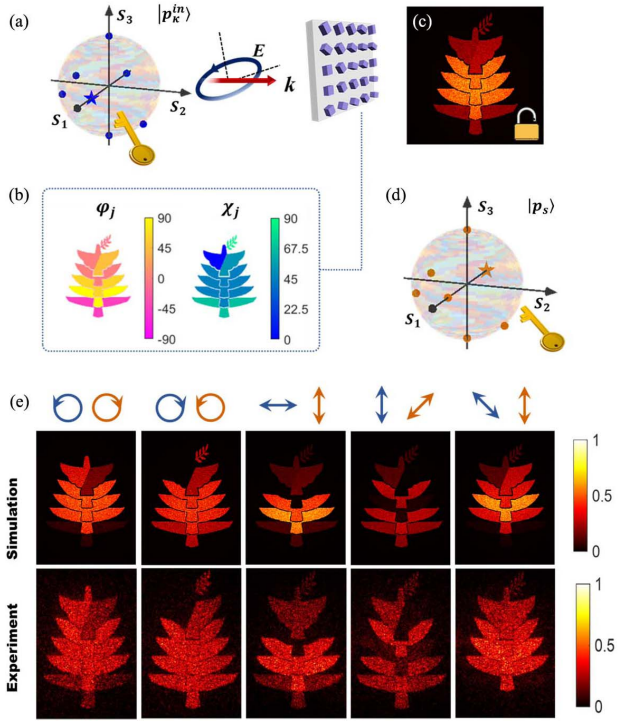

Fig. 5. Design principle of the optical encryption with double secret keys. (a) First secret key provided by input polarization states. The blue dots represent some deceptive keys, and the blue star marked at x-polarization is the correct key. (b) Polarization encryption rules encoded by φ_j and χ_j that change the phase delay and amplitude difference of vectorial images. (c) Encrypted images with only x-polarized input (first secret key). (d) Second secret key provided by output polarization states. Among those possibilities, the orange star that represents y-polarized output is the second correct key. (e) Simulated and experimental results for encrypted images at diverse input/output polarization channels (see Visualization 2).

3. CONCLUSION

In conclusion, we proposed and realized polarization multiplexed holography based on metasurfaces optimized by a hybrid genetic algorithm, which demonstrated the viability and versatility of time sequence dynamic display and optical encryption. Through full-Stokes polarization transformations and delicate metasurface design, multiple and independent input/output polarization modulations can be customized flexibly in two full-Stokes spaces. The subwavelength feature of the nanofin without coherent pixels or any spatial multiplexing not only decreases fabrication difficulties, but also ensures a larger FOV. Based on the efficient and independent phase encoding of a circular polarization basis, the output vectorial wavefront can be freely customized within an observable numerical aperture that reaches 0.80 (see Appendix A, Note 2) and conversion efficiency reaches 40.24%. The designed holographic videos with large information capacity have more displayed possibilities by using different polarization combinations. The optical encryption shows significantly improved performance compared with other

polarization encryption schemes in security and data capacity. This method is expected to be used in dynamic display and beam shaping, polarization detection, holographic tweezers, optical encryption/anticounterfeiting, and so on.

4. METHODS

Fabrication of metasurfaces. We chose α-Si as the optical material and fabricated dielectric metasurfaces on quartz substrates. The nanofin arrays have diverse cross sections and rotations. First, we deposited the α-Si film with a thickness of 600 nm by using plasma-enhanced chemical vapor deposition. Second, we made a resist layer by a spin coating method, and patterned the structures by a standard electron beam lithography process. After a process of development, a 100-nm-thick chromium layer was patterned through electron beam evaporation. Then, we used hot acetone to remove redundant overlayers, and transferred the desired pattern from chromium to silicon through inductively coupled plasma reactive ion etching. Thus, the desired metasurfaces were fabricated successfully.

APPENDIX A

This section includes the following.

Figure 6. Experimental results of sample 1 at diverse input and output polarization selections.

Figure 7. Experimental results of sample 2 at six diverse input and output polarization selections.

Figure 8. Theoretical results of sample 2 at six diverse input and output polarization selections.

Note 1. Conversion efficiency of metasurfaces (including Figs. 9 and 10).

Note 2. Numerical aperture of vectorial holography.

Note 3. Dynamic display of the designed vectorial patterns.

Other materials for this paper include Visualizations 1 and 2.

Note 1: Conversion efficiency of metasurfaces

The conversion efficiency of polarization multiplexed holography is defined as the ratio of effective diffracted power with circular polarization conversion to incident power. It equals the product of polarization conversion efficiency and holographic reconstruction efficiency. That is, $\eta_{rl} = \eta_{rl}^{h}\eta_{rl}^{p}$, $\eta_{lr} = \eta_{lr}^{h}\eta_{lr}^{p}$, where the subscripts represent incident/transmitted polarization channels, and superscripts h and p represent holography and polarization conversion, respectively.

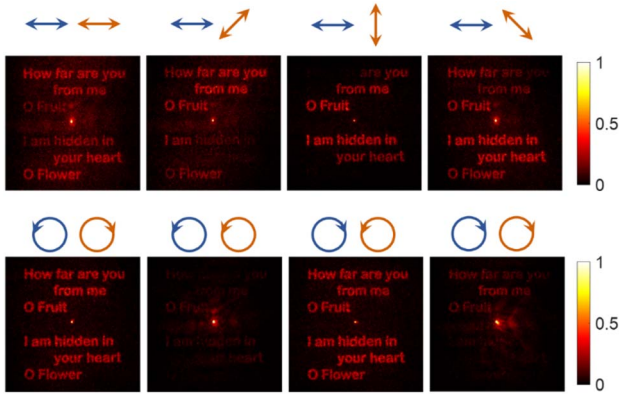

Fig. 6. Experimental results of sample 1 at diverse input and output polarization selections. The blue arrows and orange arrows are polarization states of input and output, respectively.

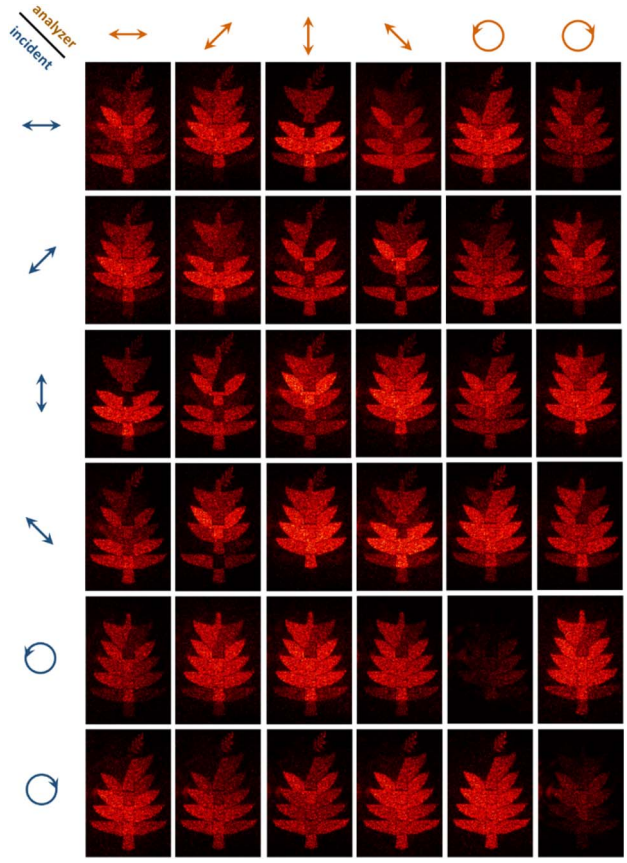

Fig. 7. Experimental results of sample 2 at six diverse input and output polarization selections. The blue arrows and orange arrows are polarization states of input and output, respectively.

First, we measured and calculated the polarization conversion efficiency of circularly polarized channels based on the optical setup shown in Fig. 3, while replacing the lens (L_2) and CCD with a power meter. Polarization conversion efficiency is defined as the ratio of transmitted power of metasurfaces to the incident power. That is, $\eta_{rl}^{p} = \frac{P_{rl}^{M}}{P_{l}^{\text{in}}}$, $\eta_{lr}^{p} = \frac{P_{lr}^{M}}{P_{r}^{\text{in}}}$, where P_{rl}^{M} is the power of metasurfaces in the $|R\rangle$ input / $|L\rangle$ output polarization channel, and so is P_{rl}^{M}; P_{l}^{in} and P_{r}^{in} represent LCP and RCP incident power, respectively. We also measured P_{rr}^{M} and P_{ll}^{M} as a reference. Incident power was measured when replacing the metasurfaces with a glass substrate of the same aperture size. As shown in Figs. 9 and 10, at a wavelength of 760 nm, η_{rl}^{p} and η_{lr}^{p} of sample 1 are 47.2% and 47.3%, and η_{rl}^{p} and η_{lr}^{p} of sample 2 reach 57.9% and 55.3%, respectively.

Furthermore, to get accurate efficiency for each vectorial component of the holographic image, we calculated the holographic reconstruction efficiency of circularly polarized channels based on an image recognition algorithm. Through such data processing, we defined the region of interest (ROI) of collected images and extracted effective information.

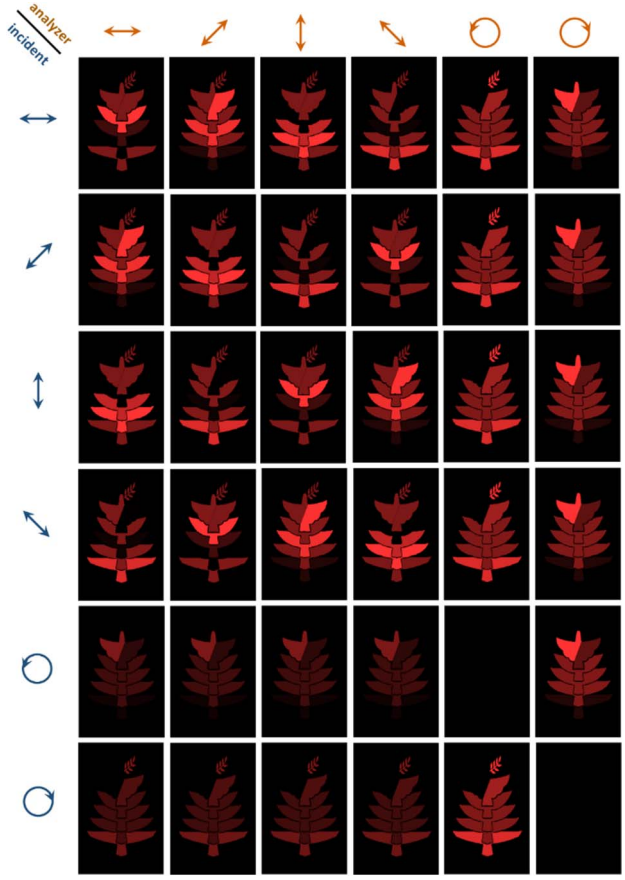

Fig. 8. Theoretical results of sample 2 at six diverse input and output polarization selections. The blue arrows and orange arrows are polarization states of input and output, respectively.

ROIs at different wavelengths were generated according to comparisons between collected images with the designed patterns, which serve as a mask to extract holographic imaging. By calculating the ratio of extracted information to the initial images as shown in Figs. 9(a) and 10(a), we obtained the

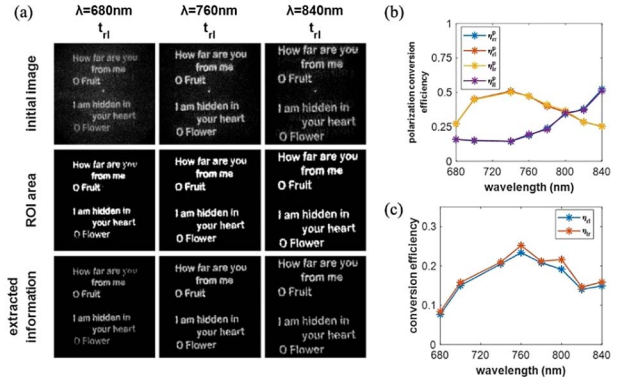

Fig. 9. Conversion efficiency and broadband behavior of sample 1. (a) Data processing of holographic construction efficiency, using ROIs generated by the algorithm to extract effective information. (b) Polarization conversion efficiencies of four circularly polarized channels. (c) Conversion efficiencies η_{rl} and η_{lr} of polarization multiplexed holography.

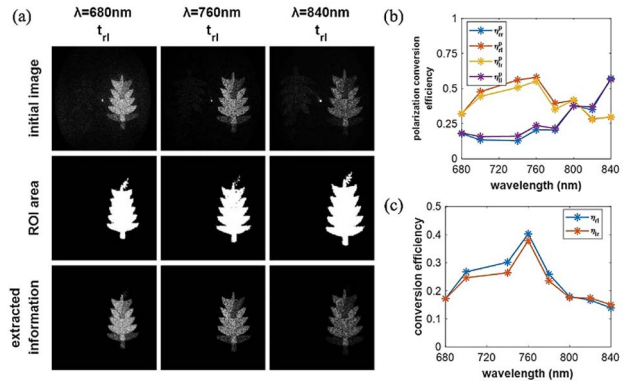

Fig. 10. Conversion efficiency and broadband behavior of sample 2. (a) Data processing of holographic construction efficiency, using ROIs generated by the algorithm to extract effective information. (b) Polarization conversion efficiencies of four circularly polarized channels. (c) Conversion efficiencies η_{rl} and η_{lr} of polarization multiplexed holography.

holographic reconstruction efficiency, and further got the effective power of polarization multiplexed holography. The results of sample 1 and sample 2 are shown in Figs. 9(c) and 10(c). At a wavelength of 760 nm, η_{rl} and η_{lr} of sample 1 are 28.68% and 29.44%, and η_{rr} and η_{ll} are 3.43% and 4.68%; η_{rl} and η_{lr} of sample 2 are 40.24% and 37.88%, and η_{rr} and η_{ll} are 13.84% and 11.70%, respectively. Because the refractive index used in the experiment is blueshifted relative to the simulated one, the experimental results in the main text and the appendix are measured at 680 nm, which almost agree with the theoretical design and demonstrate the robustness of our devices to wavelength.

Note 2. Numerical aperture of vectorial holography

The method we used ensures that each subwavelength unit is connected with all vectorial fields, which is totally different from the spatial multiplexing scheme and guarantees a larger FOV. The numerical aperture (NA) of metasurfaces is defined as

$$\mathrm{NA} = \frac{\upsilon_o \lambda}{\upsilon \times p}, \tag{A1}$$

where υ is the pixel number of the metasurfaces and the designed patterns in x direction (the computer-generated hologram we used here is based on uniform Fourier transform, and the pixel number of those in y direction is also equal to υ), p is the period of nanofins, υ_0 is half the pixel number we designed for the actual observable aperture, and λ represents wavelength. The desiged NA reaches 0.80, which shows the advantage of large information capacity, and we used an objective with 0.85 NA to collect constructed images.

Note 3. Dynamic display of the designed vectorial patterns

Here, we used varied linearly polarized input and x-polarized output selections to test the dynamic property and large information capacity of our devices. Two movies include:

Visualization 1. Dynamic display of the prose poem.

Visualization 2. Dynamic display of the optical encryption.

Funding. National Key Research and Development Program of China (2021YFA1401200); Beijing Outstanding Young Scientist Program (BJJWZYJH01201910007022); National Natural Science Foundation of China (U21A20140, 92050117); Beijing Municipal Science and Technology Commission, Administrative Commission of Zhongguancun Science Park (Z211100004821009); Fok Ying-Tong Education Foundation of China (161009).

Disclosures. The authors declare no conflicts of interest.

Data Availability. Data underlying the results presented in this paper may be obtained from the authors upon reasonable request.

REFERENCES

1. E. N. Leith and J. Upatnieks, "Reconstructed wavefronts and communication theory," J. Opt. Soc. Am. **52**, 1123–1130 (1962).
2. G. Tricoles, "Computer generated holograms: an historical review," Appl. Opt. **26**, 4351–4360 (1987).
3. Y. Peng, S. Choi, N. Padmanaban, and G. Wetzstein, "Neural holography with camera-in-the-loop training," ACM Trans. Graph. **39**, 185 (2020).
4. L. Huang, X. Chen, H. Mühlenbernd, H. Zhang, S. Chen, B. Bai, Q. Tan, G. Jin, K.-W. Cheah, and C.-W. Qiu, "Three-dimensional optical holography using a plasmonic metasurface," Nat. Commun. **4**, 2808 (2013).
5. S. Xiao, F. Zhong, H. Liu, S. Zhu, and J. Li, "Flexible coherent control of plasmonic spin-Hall effect," Nat. Commun. **6**, 8360 (2015).
6. X. Song, L. Huang, L. Sun, X. Zhang, R. Zhao, X. Li, J. Wang, B. Bai, and Y. Wang, "Near-field plasmonic beam engineering with complex amplitude modulation based on metasurface," Appl. Phys. Lett. **112**, 073104 (2018).
7. Q. Xu, X. Zhang, Y. Xu, C. Ouyang, Z. Tian, J. Gu, J. Li, S. Zhang, J. Han, and W. Zhang, "Polarization-controlled surface plasmon holography," Laser Photon. Rev. **11**, 1600212 (2017).
8. Z. L. Deng, M. Jin, X. Ye, S. Wang, T. Shi, J. Deng, N. Mao, Y. Cao, B. O. Guan, and A. Alù, "Full-color complex-amplitude vectorial holograms based on multi-freedom metasurfaces," Adv. Funct. Mater. **30**, 1910610 (2020).
9. C. Chen, S. Gao, W. Song, H. Li, S.-N. Zhu, and T. Li, "Metasurfaces with planar chiral meta-atoms for spin light manipulation," Nano Lett. **21**, 1815–1821 (2021).
10. S. Zhang, L. Huang, X. Li, R. Zhao, Q. Wei, H. Zhou, Q. Jiang, G. Geng, J. Li, and X. Li, "Dynamic display of full-Stokes vectorial holography based on metasurfaces," ACS Photon. **8**, 1746–1753 (2021).
11. E. Wang, J. Niu, Y. Liang, H. Li, Y. Hua, L. Shi, and C. Xie, "Complete control of multichannel, angle-multiplexed, and arbitrary spatially varying polarization fields," Adv. Opt. Mater. **8**, 1901674 (2020).
12. X. Zou, G. Zheng, Q. Yuan, W. Zang, R. Chen, T. Li, L. Li, S. Wang, Z. Wang, and S. Zhu, "Imaging based on metalenses," PhotoniX **1**, 2 (2020).
13. H. Wang, C. Hao, H. Lin, Y. Wang, T. Lan, C.-W. Qiu, and B. Jia, "Generation of super-resolved optical needle and multifocal array using graphene oxide metalenses," Opto-Electron. Adv. **4**, 200031 (2021).
14. Z.-L. Deng, J. Deng, X. Zhuang, S. Wang, K. Li, Y. Wang, Y. Chi, X. Ye, J. Xu, and G. P. Wang, "Diatomic metasurface for vectorial holography," Nano Lett. **18**, 2885–2892 (2018).
15. N. Yu, P. Genevet, M. A. Kats, F. Aieta, J.-P. Tetienne, F. Capasso, and Z. Gaburro, "Light propagation with phase discontinuities: generalized laws of reflection and refraction," Science **334**, 333–337 (2011).
16. S. Wang, Z.-L. Deng, Y. Wang, Q. Zhou, X. Wang, Y. Cao, B.-O. Guan, S. Xiao, and X. Li, "Arbitrary polarization conversion dichroism metasurfaces for all-in-one full Poincaré sphere polarizers," Light Sci. Appl. **10**, 24 (2021).
17. A. H. Dorrah, N. A. Rubin, A. Zaidi, M. Tamagnone, and F. Capasso, "Metasurface optics for on-demand polarization transformations along the optical path," Nat. Photonics **15**, 287–296 (2021).
18. N. A. Rubin, A. Zaidi, A. H. Dorrah, Z. Shi, and F. Capasso, "Jones matrix holography with metasurfaces," Sci. Adv. **7**, eabg7488 (2021).
19. A. Arbabi, Y. Horie, M. Bagheri, and A. Faraon, "Dielectric metasurfaces for complete control of phase and polarization with subwavelength spatial resolution and high transmission," Nat. Nanotechnol. **10**, 937–943 (2015).
20. R. Zhao, X. Xiao, G. Geng, X. Li, J. Li, X. Li, Y. Wang, and L. Huang, "Polarization and holography recording in real-and *k*-space based on dielectric metasurface," Adv. Funct. Mater. **31**, 2100406 (2021).
21. R. Zhao, B. Sain, Q. Wei, C. Tang, X. Li, T. Weiss, L. Huang, Y. Wang, and T. Zentgraf, "Multichannel vectorial holographic display and encryption," Light Sci. Appl. **7**, 95 (2018).
22. H. Ren, X. Fang, J. Jang, J. Bürger, J. Rho, and S. A. Maier, "Complex-amplitude metasurface-based orbital angular momentum holography in momentum space," Nat. Nanotechnol. **15**, 948–955 (2020).
23. H. Ren, G. Briere, X. Fang, P. Ni, R. Sawant, S. Héron, S. Chenot, S. Vézian, B. Damilano, and V. Brändli, "Metasurface orbital angular momentum holography," Nat. Commun. **10**, 2986 (2019).
24. H. Zhou, B. Sain, Y. Wang, C. Schlickriede, R. Zhao, X. Zhang, Q. Wei, X. Li, L. Huang, and T. Zentgraf, "Polarization-encrypted orbital angular momentum multiplexed metasurface holography," ACS Nano **14**, 5553–5559 (2020).
25. R. Zhao, L. Huang, and Y. Wang, "Recent advances in multi-dimensional metasurfaces holographic technologies," PhotoniX **1**, 20 (2020).
26. Y. Guo, S. Zhang, M. Pu, Q. He, J. Jin, M. Xu, Y. Zhang, P. Gao, and X. Luo, "Spin-decoupled metasurface for simultaneous detection of spin and orbital angular momenta via momentum transformation," Light Sci. Appl. **10**, 63 (2021).
27. Y. Hu, X. Luo, Y. Chen, Q. Liu, X. Li, Y. Wang, N. Liu, and H. Duan, "3D-integrated metasurfaces for full-colour holography," Light Sci. Appl. **8**, 86 (2019).
28. S. Wang, P. C. Wu, V.-C. Su, Y.-C. Lai, M.-K. Chen, H. Y. Kuo, B. H. Chen, Y. H. Chen, T.-T. Huang, and J.-H. Wang, "A broadband achromatic metalens in the visible," Nat. Nanotechnol. **13**, 227–232 (2018).
29. S. Wang, P. C. Wu, V.-C. Su, Y.-C. Lai, C. H. Chu, J.-W. Chen, S.-H. Lu, J. Chen, B. Xu, and C.-H. Kuan, "Broadband achromatic optical metasurface devices," Nat. Commun. **8**, 187 (2017).
30. W. Yilin, F. Qingbin, and X. Ting, "Design of high efficiency achromatic metalens with large operation bandwidth using bilayer architecture," Opto-Electron. Adv. **4**, 200008 (2021).
31. X. Li, L. Chen, Y. Li, X. Zhang, M. Pu, Z. Zhao, X. Ma, Y. Wang, M. Hong, and X. Luo, "Multicolor 3D meta-holography by broadband plasmonic modulation," Sci. Adv. **2**, e1601102 (2016).
32. X. Li, R. Zhao, Q. Wei, G. Geng, J. Li, S. Zhang, L. Huang, and Y. Wang, "Code division multiplexing inspired dynamic metasurface holography," Adv. Funct. Mater. **31**, 2103326 (2021).
33. L. Huang, H. Mühlenbernd, X. Li, X. Song, B. Bai, Y. Wang, and T. Zentgraf, "Broadband hybrid holographic multiplexing with geometric metasurfaces," Adv. Mater. **27**, 6444–6449 (2015).
34. I. Kim, J. Jang, G. Kim, J. Lee, T. Badloe, J. Mun, and J. Rho, "Pixelated bifunctional metasurface-driven dynamic vectorial holographic color prints for photonic security platform," Nat. Commun. **12**, 3614 (2021).
35. Q. Song, A. Baroni, R. Sawant, P. Ni, V. Brandli, S. Chenot, S. Vézian, B. Damilano, P. de Mierry, and S. Khadir, "Ptychography retrieval of fully polarized holograms from geometric-phase metasurfaces," Nat. Commun. **11**, 2651 (2020).
36. Y. Bao, L. Wen, Q. Chen, C.-W. Qiu, and B. Li, "Toward the capacity limit of 2D planar Jones matrix with a single-layer metasurface," Sci. Adv. **7**, eabh0365 (2021).
37. E. Arbabi, S. M. Kamali, A. Arbabi, and A. Faraon, "Vectorial holograms with a dielectric metasurface: ultimate polarization pattern generation," ACS Photon. **6**, 2712–2718 (2019).